Experimental study of internal gravity waves generated by supercritical topography

H. P. Zhang, B. King and Harry L. Swinney

Center for Nonlinear Dynamics and Department of Physics,

The University of Texas at Austin, Austin, Texas 78712, USA

Abstract

Oscillatory tides flowing over rough topography on the ocean floor generate internal gravity waves, which are a major source of ocean mixing. Linear inviscid theory can describe waves generated by gentle topography with slopes that are less steep than the propagation angle of the internal waves; such topography is termed subcritical. However, a clear physical picture of internal waves generated by topography with slopes steeper than the angle of internal waves (supercritical topography) is lacking. In this paper we present an experimental study at Reynolds number $\sim O(100)$ of internal gravity waves generated by a circular cylinder that oscillates horizontally at a frequency Ω. Fundamental waves of frequency Ω emanate from locations on the cylinder where the topographic slope equals the slope of internal waves. For small oscillating amplitude A (weak forcing), our experimental results compare well with predictions of the *viscous* linear theory of Hurley and Keady (1997). The width of the wave beams is determined by competition between forcing and viscous smoothing, and hydrodynamic screening of the steep part of the topography extends the cylinder's horizontal length scale. Beyond the weak forcing regime, harmonic waves of frequency $n\Omega$ (with integer $n > 1$ and $n\Omega < N$, where N is the buoyancy frequency) are generated by nonlinear interaction involving the overlapping fundamental waves and direct forcing of the cylinder. For moderate forcing we find that the intensity of the fundamental and second harmonic waves scales linearly and quadratically with A, respectively.

I. INTRODUCTION

Away from shallow, well-mixed surface regions, most of the ocean is stratified by salinity and temperature [1, 2]. In the deep ocean, internal gravity waves are created by oscillatory tides flowing over bottom topography such as underwater mountains and ridges [1, 3]. This can be easily appreciated in a reference frame moving with the tides; the bottom topography then acts like an oscillating wavemaker which generates waves. These tide-generated internal gravity waves, also called internal tides, are believed to one of the major sources of deep-ocean mixing, which is one of the least understood, yet crucial, aspects of ocean circulation models [1, 5, 6]. Therefore, a considerable effort is now underway to understand better the processes involved in internal gravity wave generation, propagation, and dissipation [1, 3].

In a uniformly stratified nonrotating fluid, internal gravity waves propagate obliquely with an angle μ with respect to the horizontal, where [4]

$$\tan\mu = \sqrt{\frac{\Omega^2}{N^2-\Omega^2}}, \tag{1}$$

Ω is the wave frequency, and N is the buoyancy frequency. Bottom topography can be characterized as supercritical or subcritical according to the "criticality parameter," $\varepsilon = S_m/\tan\mu$, where S_m is the maximal topographic slope. The topography is supercritical (subcritical) when $\varepsilon > 1$ ($\varepsilon < 1$). Another nondimensional parameter [3] related to spatial scales is the "excursion parameter," $\beta = A/l$, which is the ratio of forcing amplitude of the wavemaker, $A = u_\circ/\Omega$ (where $u_\circ$ is the maximal oscillating velocity), to the horizontal scale of the topography l.

The internal gravity wave generation problem is difficult to treat analytically in general because both the governing hydrodynamic equations and the boundary condition on the topography are nonlinear. However, the problem is greatly simplified for gentle subcritical topography, for which inviscid theory [3, 7, 8] predicts wave fields with small spatial gradients and smooth variation over the scale of the topography. Small spatial gradients means that both the viscous ($\nu\nabla^2\vec{u}$) and nonlinear ($\vec{u}\cdot\nabla)\,\vec{u}$ terms are small. However, as the steepness of the topography increases, wave fields and their spatial gradients grow large along the wave characteristics, which are are lines that are in the wave propagation direction and tangent to the topographic surface. The fields and gradients eventually diverge for waves generated by supercritical topography, $\varepsilon > 1$, where the assumptions of linear and inviscid

flow fail [10, 11, 16]. The unphysical divergent wave fields for supercritical topography are a consequence of the inviscid assumption. Hurley and Keady [9] presented an approximate *viscous* linear theory of internal gravity waves generated by an oscillating circular cylinder in a viscous fluid. The topographic slope of the top and bottom halves of a cylinder ranges from 0 to ∞; thus it is supercritical for internal gravity waves propagating in any direction. The Hurley-Keady theory shows that the viscous term can smooth large gradients and prevent the wave fields from diverging. No theoretical analysis has been done for the full nonlinear equations, but strong nonlinear effects have been reported in nonlinear numerical studies of supercritical topography [21–23].

The inviscid assumption fails for supercritical topography also because of the free-slip boundary condition, which assumes the topographic surface is a streamline of the flow. Studies of lee wave generation have shown that steep topography in a strongly stratified fluid usually blocks some upstream fluid and causes flow to separate from the topographic surface; hence the free-slip boundary condition is invalidated [24, 25]. The failure of the inviscid assumption is quantified by a nondimensional number $L = NH/u_*$, where H is the maximum height of topography and u_* is a typical flow velocity. The lee wave studies have shown that when L is larger than a critical number between 0.5 and 1, strong stratification greatly inhibits vertical motion, blocking a fluid particle from rising over the topography [24, 25].

We present here a laboratory experiment designed to study viscous and nonlinear effects for internal gravity waves generated by an oscillating cylinder (with small excursion parameter, $\beta \ll 1$) in a non-rotating stratified fluid (with constant buoyancy frequency N). Several previous studies used an oscillating circular cylinder to excite internal gravity waves [12–15]. Those studies examined the structure of the propagating waves in the far field; details of flow-topography interaction in the near field were not studied. Further, the studies used small cylinders, resulting in small Reynolds number, $Re = u_\circ D/\nu \sim O(10)$, where ν is the kinematic viscosity and D the cylinder diameter. The present experiment examines both near and far fields for $Re \sim O(100)$. Our velocity field measurements reveal that for weak forcing, the flow is essentially linear, and the observations, including blocking (since $L > 1$), are in good accord with the viscous theory of Hurley and Keady [9]. Beyond the weak forcing regime, nonlinear interactions generate harmonics $n\Omega$ for integer n such that $n > 1$ and $n\Omega < N$.

The paper is organized as follows. Section II reviews the linear viscous theory of Hurley

and Keady, and Section III describes the experimental system. Sections IV and V present results from the weak and moderate forcing regimes, respectively. Oceanographic implications of our results are discussed in Section V.

II. THEORY

Hurley and Keady [9] proposed an approximate viscous solution for internal gravity waves generated by a circular cylinder (radius r) oscillating horizontally $u = u_\circ \exp(i\Omega t)$ in a Boussinesq fluid with uniform stratification ($N = constant$). The coordinate system in the laboratory frame has the x-axis horizontal and the y-axis vertical, and the origin is at the center of the cylinder's equilibrium position. Internal waves propagate in a direction defined by the dispersion relation, Eq. (1), and form an X pattern. We define two beam coordinate frames, $S_+O\sigma_+$ and $S_-O\sigma_-$, where each has one axis (S_+ or S_-) directed along the wave beam and the other axis (σ_+ or σ_-) perpendicular to the wave beam (Fig. 1). The coordinate frames are related by

$$\sigma_+ = x\sin(\mu) - y\cos(\mu), \quad s_+ = \ x\cos(\mu) + y\sin(\mu), \tag{2}$$

$$\sigma_- = x\sin(\mu) + y\cos(\mu), \quad s_- = -x\cos(\mu) + y\sin(\mu). \tag{3}$$

Assuming the wave structure is uniform along the length of the cylinder and the fluid is incompressible, the two-dimensional wave motion is described by the stream function $\Psi(x, y, t) = \psi(x, y)exp(-i\Omega t)$. Once $\psi(x, y)$ is determined, the horizontal (u) and vertical (v) components of the velocity field are given by

$$u(x, y, t) = -\frac{\partial\psi(x, y)}{\partial y}exp(-i\Omega t), \quad v(x, y, t) = \frac{\partial\psi(x, y)}{\partial x}exp(-i\Omega t). \tag{4}$$

The vorticity field,

$$\omega(x, y, t) = \bigtriangledown^2\Psi(x, y, t),$$

has only one component in our essentially two-dimensional flow, and the wave amplitude of vorticity field is defined as

$$\omega_\circ(x, y) = \bigtriangledown^2\psi(x, y).$$

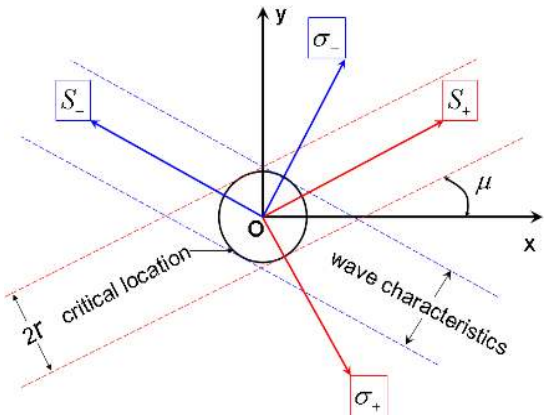

FIG. 1: Coordinate frames. The laboratory frame is xOy with y-axis vertical. Internal gravity waves propagate along the directions of the wave characteristics, shown by dashed lines. The wave characteristics and the cylinder surface coincide at the critical locations. The two beam frames are $S_+O\sigma_+$ and $S_-O\sigma_-$.

The Navier–Stokes and continuity equations are linearized and simplified to give a single fourth order partial differential equation in $\psi(x, y)$:

$$\eta^2 \frac{\partial^2 \psi(x,y)}{\partial x^2} - \frac{\partial^2 \psi(x,y)}{\partial y^2} + \frac{i\nu}{\Omega} \bigtriangledown^4 \psi(x,y) = 0, \tag{5}$$

where

$$\eta^2 = N^2/\Omega^2 - 1.$$

The no-slip boundary condition is assumed on the cylinder surface, whose spatial position does not change in the limit of $\beta \to 0$,

$$\psi(x,y)|_{cylinder} = -u_\circ y. \tag{6}$$

If viscosity is neglected, Eq. (5) becomes

$$\eta^2 \frac{\partial^2 \psi(x,y)}{\partial x^2} - \frac{\partial^2 \psi(x,y)}{\partial y^2} = 0, \tag{7}$$

which can be solved exactly together with the boundary condition, Eq. (6), to obtain the exact inviscid solution,

$$\psi^{in}(x,y) = \psi^{in}_+(\sigma_+) + \psi^{in}_-(\sigma_-)$$

and

$$\psi^{in}_+(\sigma_+) = r\alpha_+ \left\{ \frac{\sigma_+}{r} - \left(\frac{\sigma_+^2}{r^2} - 1 \right)^{1/2} \right\} \tag{8}$$

$$\psi_{-}^{in}(\sigma_{-}) = r\alpha_{-}\left\{\frac{\sigma_{-}}{r} - \left(\frac{\sigma_{-}^2}{r^2} - 1\right)^{1/2}\right\}$$

where α_+ and α_- are:

$$\alpha_{+} = \frac{1}{2}\left[+u_{\circ}\cos(\mu) - iu_{\circ}\sin(\mu)\right], \tag{9}$$

$$\alpha_{-} = \frac{1}{2}\left[-u_{\circ}\cos(\mu) + iu_{\circ}\sin(\mu)\right]. \tag{10}$$

A major problem with the inviscid solution is that the velocity field, calculated by Eqs. (4) and (8), diverges on the wave characteristics, $\sigma_+ = \pm r$ and $\sigma_- = \pm r$. This divergence on wave characteristics is common in inviscid theories and simulations for supercritical topography [10, 11, 16, 17].

Based on the inviscid solution, Hurley and Keady [9] proposed an approximate viscous solution under the boundary-layer approximation, which assumes that across-beam variations are more significant than along-beam variations. The viscous solution is also expressed in the beam frames:

$$\psi(x, y) = \psi_{+}(\sigma_{+}, s_{+}) + \psi_{-}(\sigma_{-}, s_{-})$$

where

$$\psi_{+}(\sigma_{+}, s_{+}) = \mp i\alpha_{+}r\int_0^{\infty}\frac{J_1(K)}{K}\exp(\mp K^3\lambda\frac{s_{+}}{r} \pm iK\frac{\sigma_{+}}{r})dK, \quad \pm s_{+} > 0 \tag{11}$$

$$\psi_{-}(\sigma_{-}, s_{-}) = \pm i\alpha_{-}r\int_0^{\infty}\frac{J_1(K)}{K}\exp(\mp K^3\lambda\frac{s_{-}}{r} \mp iK\frac{\sigma_{-}}{r})dK, \quad \pm s_{-} > 0 \tag{12}$$

where $J_1(K)$ is the Bessel function of the first kind, and the parameter

$$\lambda = \frac{\nu}{2r^2\Omega\eta},$$

measures the strength of viscous effects. λ is small in our experiments, e.g., $\lambda = 7.5 \times 10^{-4}$ for $r = 2.54$ cm, $\Omega = 0.38$ rad/s, $\Omega/N = 0.34$ and $\nu = 0.01$ cm^2/s. The small λ ensures that the variations along the beam direction are much smaller than across the beam direction in most regions, i.e., the boundary-layer approximation is consistent with the solution [9].

Focusing on the waves in the first and third quadrant, Eq. (11), we see that the viscous solution depends on two nondimensional coordinates, the along-beam direction,

$$\Delta = \lambda\frac{s_{+}}{r} = \left(\frac{\nu}{2\Omega\eta}\right)\frac{s_{+}}{r^3}, \tag{13}$$

and the cross-beam direction,

$$w = \frac{\sigma_{+}}{r}.$$

Since $\Delta \propto 1/r^3$ while Δ varies linearly with s_+, we can explore the dependence on Δ more efficiently by changing r than changing s_+.

The solutions (11) and (12) are symmetric and guarantee that the vertical velocity on the x axis is always zero. We use the boundary layer approximation and calculate the velocity component only along the beam direction; however, taking into account much smaller cross-beam velocity would not change the conclusions. The along-beam velocities are:

$$V_+(\sigma_+, s_+) = +\alpha_+ \int_0^\infty J_1(K) \exp(\mp K^3 \lambda \frac{s_+}{r} \pm iK\frac{\sigma_+}{r}) dK, \quad \pm s_+ > 0 \tag{14}$$

$$V_-(\sigma_-, s_-) = -\alpha_+ \int_0^\infty J_1(K) \exp(\mp K^3 \lambda \frac{s_-}{r} \mp iK\frac{\sigma_-}{r}) dK, \quad \pm s_- > 0 \tag{15}$$

where we have used $\alpha_+ = -\alpha_-$, as seen from Eqs. (9) and (10). For an arbitrary point on the x axis $(x^*, 0)$, we have coordinates in the beam frames $\sigma_+^* = \sigma_-^* = x^* \sin\mu$ and $s_+^* = -s_-^* = x^* \cos\mu$. Equations (14) and (15) give $V_+(\sigma_+^*, s_+^*) = -V_-(\sigma_-^*, s_-^*)$; therefore,

$$\vec{V}(x^*, 0) = V_+(\sigma_+^*, s_+^*)\widehat{s_+} + V_-(\sigma_-^*, s_-^*)\widehat{s_-} = 2V_+(\sigma_+^*, s_+^*)\cos(\mu)\widehat{x}$$

has only horizontal components. This symmetric property justifies the relevance of the theory to the oceanic conditions, where the boundary consists of both mountains and flat sea floor. Figure 2 illustrates the generation of internal gravity waves by a semicircular mountain on a flat sea floor. Because the oscillatory boundary layer on a *flat* surface is thin, $\delta \sim (\nu/\omega)^{1/2}$[29, 30], the no-slip boundary condition on the sea floor can be approximated by free-slip one, which is automatically satisfied in the theory. Therefore, Eqs. (11) and (12) describe internal gravity waves for $y > 0$ that satisfy the boundary conditions both on the surface of the semicircular mountain and on the ocean floor.

III. EXPERIMENTAL SET-UP

The experiments are performed in a 95 cm wide, 45 cm thick, and 60 cm high glass tank, as illustrated in Fig. 3. Blocksom-filter matting (from www.aquaticeco.com) on the tank walls greatly reduces wave reflections at the boundaries. A circular cylinder is immersed in the tank and oscillated horizontally under computer control. Four different cylinder sizes are used: $r = 0.95$, 1.59, 2.54, and 3.81 cm. The tank is filled with an uniformly stratified sugar solution using a "double bucket" system [18]. The buoyancy frequency ($N = 1.1$ rad/s

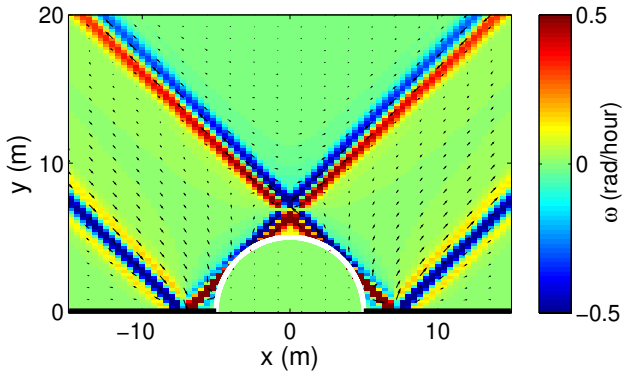

FIG. 2: Internal gravity waves generated by a semi-circular mountain (white line) on the sea floor (black lines). The mountain is centered at $(0, 0)$ and the sea floor is at $y = 0$. The wave fields are calculated from the viscous theory of Hurley and Keady, with $r = 5$ m, $N/2\pi = 0.5$ cycles/hour and $\Omega/2\pi = 0.35$ cycles/hour. The vorticity and velocity fields are represented by colorcoding and vectors respectively.

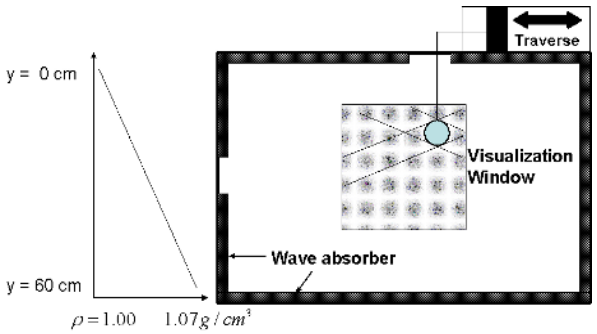

FIG. 3: Front view of experimental system showing the oscillating cylinder, which generates internal waves. Velocities are measured in the visualization window. Wave reflections at the boundaries are greatly reduced by Blocksom-filter matting on the tank walls.

in all experiments) is determined by withdrawing small amounts of fluid at different heights and measuring the density with an Anton Paar density meter.

A two-dimensional Particle Image Velocimetry (PIV) system is used to measure the velocity field in a 30 cm × 30 cm visualization window (Fig. 3). Images are obtained using a CCD camera with a resolution of 1004 x 1004 pixels and a 10-bit dynamic range. The laser beam is spread by a cylindrical lens into a light sheet approximately 0.5 mm thick in

the visualization window. The fluid is seeded with TiO_2 particles, which are denser than the sugar-water solution, but the sedimentation (with speed ~ 1 cm/hour) is negligible during a velocity measurement. Images are analyzed using the CIV velocity image correlation algorithm [26], which determines the displacement of particles in a small region by cross correlating a pair of consecutive images. We obtain a velocity field on a 100×100 grid with a rms error less than 5%. The time separation between image pairs is typically 1/20 of the wave period; 20 velocity fields are obtained per wave period. In the moderate and strong forcing regime, Fourier decompositions of time series of $\vec{u}(x, y, t)$ and $\vec{\omega}(x, y, t)$ are used to separate the contributions from the fundamental and harmonics (see Section V.B). Because of the symmetry between waves in different quadrants, we obtain maximal spatial resolution by measuring only the lower-left quadrant.

IV. WEAK FORCING REGIME

In the weak forcing regime (excursion parameter $\beta = A/r \ll 1$), the strength of the superharmonic waves is much less than the fundamental waves. We compare our observations in this regime with the viscous theory of Hurley and Keady [9].

A. Near field

We examine first the flow near the cylinder, where $\Delta = (\nu/2\Omega\eta)s_+/r^3 < 3.5 \times 10^{-4}$. The measured velocity and vorticity fields compare well with theory, as Fig. 4 illustrates; note that the theory does not involve any fit parameter. Internal gravity waves, shown by the vorticity band, emanate from critical locations on the cylinder and propagate at an angle determined by the dispersion relation, Eq. (1). The fluid in the region between the waves and the cylinder surface has horizontal velocity nearly the same as the cylinder. A similar blocking of flow occurs at other moments of the oscillating cycle (cf. Sections IV.B and V.B). This blocking effect is expected to be generic property of any supercritical topography oscillating with small excursion parameter β. The L number introduced in the introduction can be rewritten as

$$L = \frac{NH}{u_\circ} = \frac{NH}{\Omega l}\left(\frac{1}{\beta}\right). \tag{16}$$

Since the forcing frequency Ω and topographic height H are usually the same order as N and l, respectively, if $\beta \ll 1$, then $L \gg 1$; hence stratification dominates kinematic effects, and blocking is strong. To test this idea, we oscillated a vertical flat plate with the other experimental parameters the same as used in Fig. 4. The vertical plate can be approximated by an ellipse with a very large aspect ratio, which has large supercritical topographic slope everywhere except at the two ends, where the critical locations are located. The instantaneous velocity and vorticity fields, shown in Fig. 5, are very similar to those in Fig. 4 (a) and (b): waves emanate from the critical locations and fluid is blocked in the region bounded by the plate and the waves.

B. Bimodal region

Just beyond the near field, two distinct waves are observed in the same quadrant, as shown in Fig. 6, which was obtained for the same experimental conditions as in Fig. 4 but in a larger visualization window. The observed bimodal wave profile is in good accord with the viscous theory of Hurley and Keady [9].

In the bimodal regime, the wave amplitude peaks on the wave characteristics and the beam width, defined by the vorticity bands, is about 1 cm (full width at half maximum), 25% of the cylinder radius. This is very different from the prediction of inviscid theories [10, 11, 16], where the beam width is infinitesimally small. In the experiment and the viscous theory, the viscous term, $\nu\nabla^2\vec{u}$, smooths large gradients and prevents wave fields from diverging. Therefore, for waves generated by supercritical topography, it is a competition between the viscous smoothing effect and the forcing, not the actual dimension of the topography that determines the beam width. This is different from the case of subcritical topography, where the beam width is directly related to the dimension of the topography.

C. The bi-to-unimodal transition

The cross-beam profile (Eqs. 11 and 12) depends on the nondimensional along-beam coordinate Δ. For small Δ the profile is bimodal, but at $\Delta \simeq 10^{-2}$ the two parallel nearby beams merge due to viscous smoothing and the profile develops a single maximum. Beam profiles in the bimodal, transition, and unimodal regimes are shown in Fig. 7. Viscous

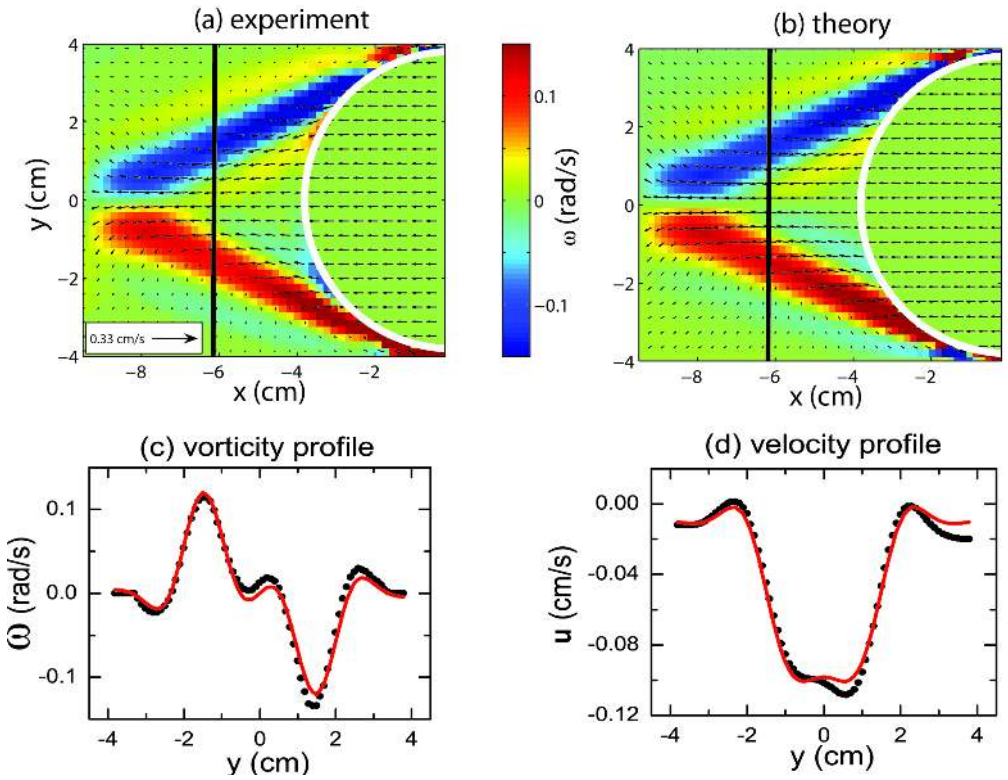

FIG. 4: (Color online) (a) and (b), velocity (arrows) and vorticity (color bar) fields in near field, respectively, from experiment and theory [9] at the instant when the oscillating cylinder passes the equilibrium position from right to left. (c) and (d), vorticity ω and horizontal velocity u profiles along $x = 6.2$ cm (vertical black lines in (a) and (b)); the solid lines are from theory and the points are from experiment. Inside the cylinder (white semi-circle) the velocity is set to the cylinder velocity and the vorticity is set to zero. Parameter values: buoyancy frequency $N = 1.1$ rad/s, wave frequency $\Omega = 0.44$ rad/s, cylinder radius $r = 3.81$ cm, and cylinder oscillation amplitude $A = 0.19$ cm.

damping leads to decreasing nondimensional wave amplitude with increasing nondimensional along-beam coordinate Δ.

The good correspondence between experiment and theory in Figs. 4, 6 and 7 indicates that the boundary layer approximation used in the theory is valid in our experiment and may be used to derive results for other topographic shapes. The small discrepancy between theory and experiment in Figs. 4 and 6 likely arises from the weak second harmonic waves, which for the experimental conditions are about one-tenth as strong as the fundamental

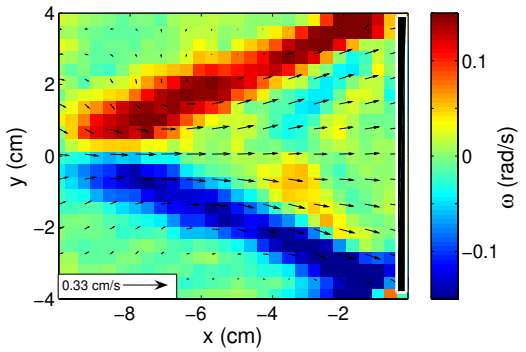

FIG. 5: (Color online) Instantaneous velocity and vorticity fields generated by a horizontally oscillating vertical plate (7.9 cm × 20 cm × 0.5 cm) at the instant when the plate passes the equilibrium position from the left to the right. The plate surface is shown by a white line. The parameter values are the same as in Fig. 4, and the velocity and vorticity fields are represented in the same way as in that figure.

waves; the harmonics are not included in the theory.

V. BEYOND THE WEAK FORCING REGIME

Beyond the weak forcing regime, superharmonic waves, not predicted by the linear theory of Hurley and Keady [9], become strong. In a experiment with a forcing amplitude twice as large as in Fig. 6, both the fundamental and the second harmonic can be seen (Fig. 8(a)). Our choice of $\Omega/N = 0.4$ allows no harmonics higher than the second to be generated. The measured fields decomposed by Fourier analysis into fundamental and the second harmonic components are shown in Fig. 8(b) and (c).

A. Generation mechanism of the second harmonic waves

Tabaei *et al.* [20] have shown that, because the phase velocity is perpendicular to particle motion $\vec{u}$, the nonlinear term, $(\vec{u}\cdot\nabla)\,\vec{u}$, is small for any freely-propagating internal wave beams of single frequency Ω in a stratified fluid with constant N and weak viscosity. However, nonlinear effects leading to superharmonic waves can be strong in the overlapping region of wave beams [20]. Superharmonic waves have been observed in numerical simulations of the

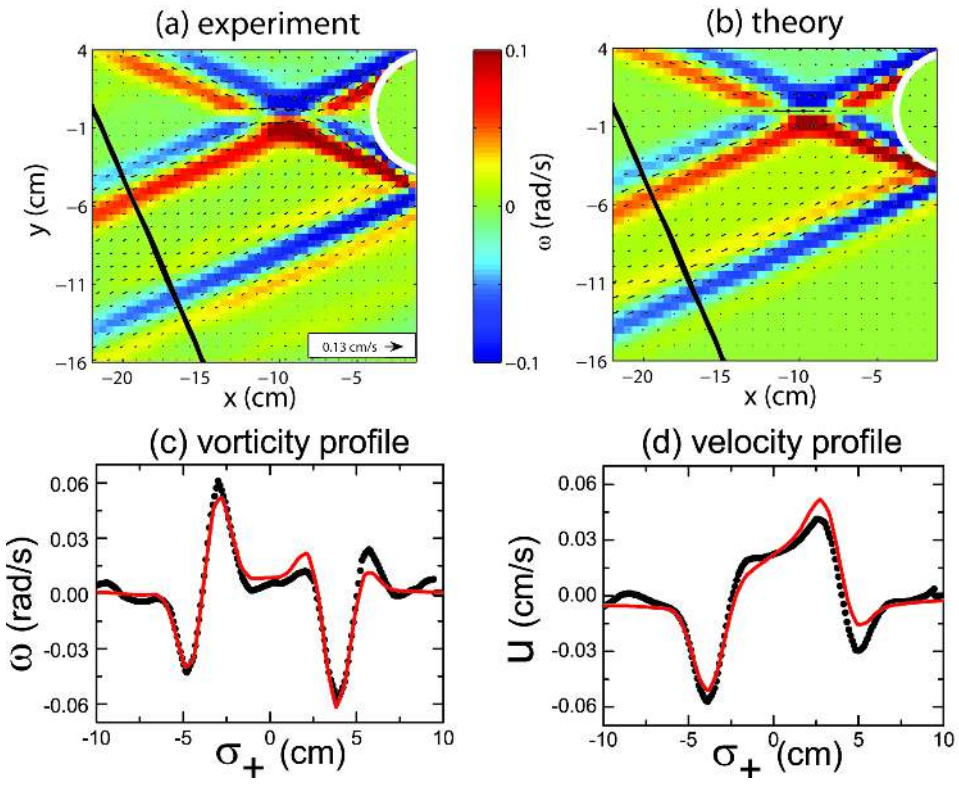

FIG. 6: (Color online) velocity (arrows) and vorticity (color bar) fields in bimodal region from (a) experiment and (b) theory[9] at the instant when the oscillating cylinder passes its equilibrium position from right to left. The field of view is larger than in Fig. 4, but the parameter values and the representation of the fields are the same. (c) and (d), vorticity and horizontal velocity profiles along the black lines, $S_+ = -14.2$ cm in the beam frame.

nonlinear equations [21–23] and in laboratory experiments [27, 28], where superharmonic waves were generated by interactions between incoming and reflected waves near a planar boundary.

In our experiments, second harmonic waves emanate from two regions where the fundamental waves overlap, which are centered roughly at (−10 cm, 0 cm) and (0 cm, −6 cm) in the laboratory frame. However, these two regions are not far enough away from the cylinder to be free of its direct influence. For example, the left region at $(-10, 0)$, though far from the actual cylinder surface, is at the edge of the blocked fluid. Therefore, the generation of harmonics for our experimental conditions involves both the fundamental waves and direct forcing from the cylinder.

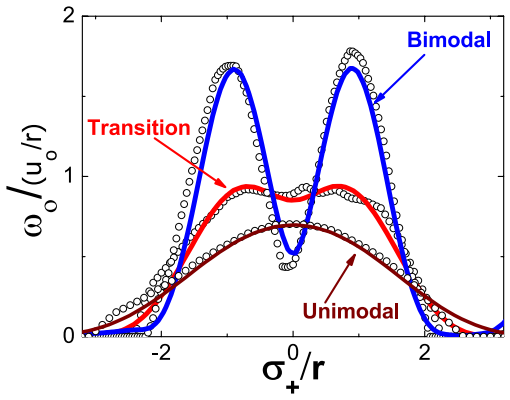

FIG. 7: (Color online) Transion from bimodal to unimodal cross-beam profiles of nondimentioanal vorticity amplitude, $\omega_\circ r/u_\circ$, as a function of the nondimentional cross-beam coordinate σ_+/r in the beam frame $S_+O\sigma_+$ (experiment, open circles; theory[9], lines). The unimodal, transitional, and bimodal profiles correspond to nondimensional along-beam coordinate $\Delta = \lambda\frac{s_+}{r}$ values of 5.4×10^{-3}, 1.7×10^{-2} and 5.3×10^{-2}, respectively. Experimental results are open circles and theoretical predictions are lines. Parameter values: bimodal, $r = 2.54$ cm and $S_+ = 7r$; transition, $r = 1.59$ cm and $S_+ = 9r$; unimodal, $r = 0.95$ cm and $S_+ = 10r$ (in each case $\Omega = 0.38$ rad/s and $N = 1.1$ rad/s)

The group velocity of the second harmonic waves, shown by C_g in Fig. 8(c), indicates that energy radiates outward from the generation regions. However, these generation sites are different from the oscillating physical wavemaker, and harmonics are not generated in an X-pattern corresponding to the four possible directions defined by the dispersion relation. For example, only two second harmonic waves propagating to the left emanate from the overlapping region at $(-10, 0)$ (Fig. 8(a)). This observation agrees with the prediction of the superharmonic generation from pure wave-wave interaction (see Fig. 7(e) in [20]).

B. Structure of the waves

We measure the cross-beam profiles of the vorticity amplitude $\omega_\circ$ and the instantaneous vorticity field ω along the black lines ($S_+ = -10.5$ cm in the beam frame) in Fig. 8(b) and (c) to study the structure of the waves. The cross-beam profile of the vorticity amplitude $\omega_\circ$

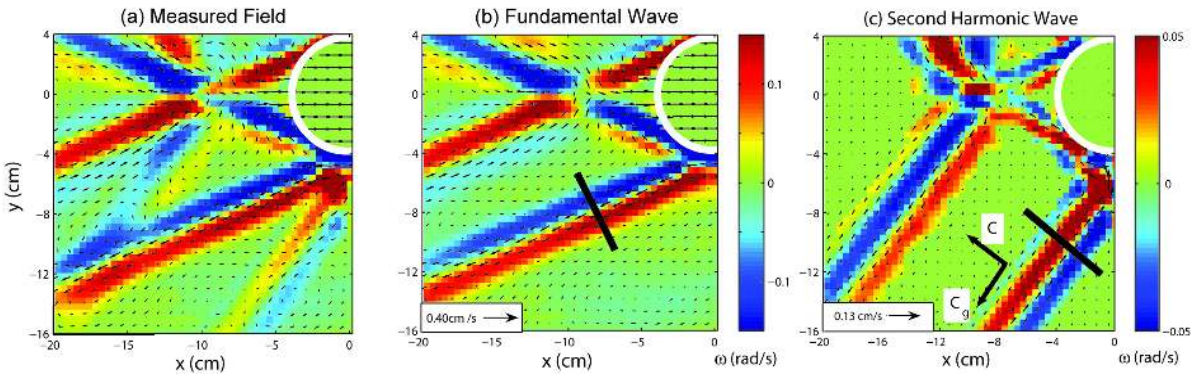

FIG. 8: (Color online) Decomposition of (a) the total vorticity and velocity fields into (b) fundamental (0.44 rad/s) and (c) the second harmonic (0.88 rad/s) components, at the instant when the cylinder moves past its equilibrium position from the left to the right. The velocity and vorticity fields are represented in the same way as in Fig. 4. The cross-beam profiles along the black lines in (b) and (c) are shown in Figs 9 and 10. Note the different velocity and vorticity scales in (a,b) and (c). Parameter values: $N = 1.1$ rad/s, $\Omega = 0.44$ rad/s, $r = 3.81$ cm and $A = 0.38$ cm.

of the fundamental wave is compared in Fig. 9(a) with the linear viscous theory of Hurley and Keady. Despite the presence of a strong second harmonic, the theory agrees with the measurements surprisingly well, differing only in the tail region. However, the harmonic causes a temporal phase change: the measured vorticity field profile agrees with the theory only when the theoretical prediction is forwarded in time by $\Delta t_1 = 0.22T$, where $T = 2\pi/\Omega$ is the period of the fundamental wave (see Fig. 9(b)).

The cross-beam profiles of the fundamental and second harmonic waves are compared in Fig. 10. The vorticity profile of the second harmonic wave, multiplied by 3, matches the profile of the vorticity amplitude of the fundamental wave, as Fig. 9(a) shows. Further, the instantaneous vorticity field for the second harmonic, if multiplied by 3 and forwarded in time by $\Delta t_2 = 0.3T$, matches the fundamental wave, as shown in Fig. 9(b). We conclude that the second harmonic wave differs from the fundamental only by its strength and a temporal phase factor.

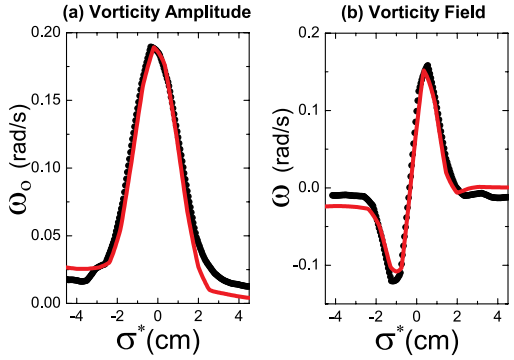

FIG. 9: (Color online) Comparison of the fundamental wave from experiment (black points) with theory (solid curves): cross-beam profiles of (a) the vorticity amplitude and (b) the vorticity field, determined at $S_+ = -10.5$ cm in the beam frame (i.e., along the black lines in Fig. 8(b)). The origin of cross-beam σ axis is shifted to be at the peak of the profiles of the vorticity amplitude, and the new axis is denoted as σ^*. In (b) the profile is forwarded in time by $\Delta t_1 = 0.22T$ (see text).

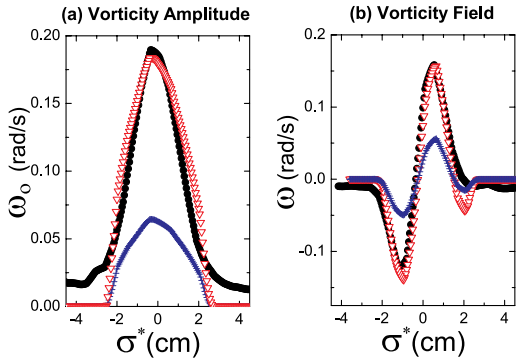

FIG. 10: (Color online) Comparison of the cross-beam profiles of the fundamental (black circles), second harmonic (blue triangles), and the second harmonic multiplied by 3 (red triangles): (a) vorticity amplitude and (b) instantaneous vorticity field, measured along the black lines in Fig. 8. The second harmonic multiplied by 3 matches the fundamental, where in (b) the second harmonic has also been shifted in time by $\Delta t_2 = 0.3T$.

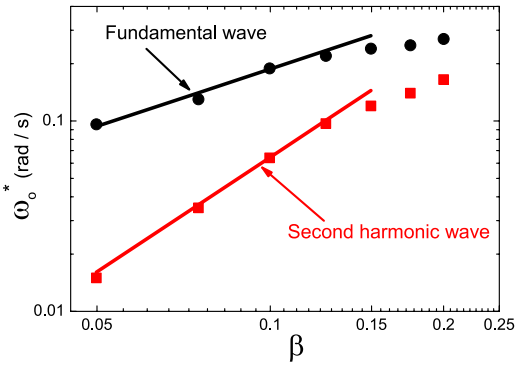

FIG. 11: (Color online) The strength of the fundmental and second harmonic waves, $\omega_\circ(\sigma^* = 0, S_+ = 10.5)$ (see text), as a function of the forcing, $\beta = A/r$. At intermediate forcing levels the fundamental depends linearly on β, while the second harmonic has a quadratic dependence.

C. Forcing amplitude dependence

The strength of both fundamental and the second harmonic waves depends strongly on the forcing amplitude. We choose the maximal value of the vorticity amplitude in the cross-beam profiles at $S_+ = -10.5$ cm, which are shown in Fig. 9 (a) and Fig. 10 (a) for fundamental and harmonic waves with excursion parameter $\beta = 0.1$, to represent the strength of waves. The chosen values, $\omega_\circ^* = \omega_\circ(\sigma^* = 0, S_+ = -10.5$ cm), are then plotted as a function of β in Fig. 11. For $\beta < 0.15$, the strengths of the fundamental and the second harmonic waves scale linearly and quadratically with β, respectively, which suggests that the generation of harmonics may be explained by a weakly nonlinear theory. Both scaling laws, also reported in [12], saturate for $\beta > 0.15$, where many frequency components are excited around the cylinder. We have tried other quantities, such as average vorticity amplitude along center lines, to represent the strength of waves. Since the spatial structures of wave amplitudes have weak dependence on β, similar results are obtained as using $\omega_\circ^* = \omega_\circ(\sigma^* = 0, S_+ = -10.5$ cm).

VI. DISCUSSION AND CONCLUSIONS

Our experiments reveal a clear physical picture of internal gravity waves generated by supercritical topography. In the weak forcing regime, linear dynamics dominates and only fundamental waves of Ω are observed. The fundamental waves are generated by direct flow-topography interaction and emanate from the critical locations. The width of the wave beam is determined by competition between the forcing and viscous smoothing. A significant amount of fluid is blocked upstream by the topography as a consequence of the strong stratification and the no-slip boundary condition. The experimental results in the weak forcing regime compare well with the predictions from the viscous linear theory of Hurley and Keady[9]. Beyond the weak forcing regime, superharmonic waves of frequency $n\Omega$ (for integer n such that $n > 1$ and $n\Omega < N$) are generated by nonlinear interaction of overlapping fundamental waves and direct forcing of the cylinder. The intensities of the fundamental and the second harmonic scale linearly and quadratically, respectively, with forcing amplitude for moderate forcing.

The blocking phenomenon, observed in Figs. 4 and 5, is expected to be generic for any supercritical topography, as reasoned in Section IV.A. The blocked fluid hydrodynamically screens the steep part of the topography, increases the horizontal length scale, and makes the topography less "supercritical". This screening effect and the observation that the critical locations are the strongest wave generation sites on the topography lead us to conjecture that the properties of the internal gravity waves are mainly determined by the *local* topographic properties such as the radius of curvature at the critical locations.

The strong superharmonic waves in our experiments with $\beta < 1$ invalidates the common assumption that a small excursion parameter $\beta < 1$ justifies the linearization of the dynamical equations in analyses of internal wave generation [3, 8–10, 16]. This assumption is based on Bell's classic work [7], where superharmonic waves are generated by the advection of the boundary conditions only when the excursion parameter is large, $\beta \geqslant 1$. However, the dynamical equations in Bell's work are linearized, which means that Bell's work takes into account only the nonlinearity arising from the boundary condition, not from the dynamical equations. Our experiment, together with other work [21–23], demonstrates the necessity of taking into account the nonlinearity from wave-wave interaction; the full nonlinear dynamical equations should be used to model internal gravity waves generated by supercritical

topography. One implication of using nonlinear dynamical equations is that internal gravity waves generated by different tidal components, such as the lunar semi-diurnal tide M2 and the diurnal tide M1, are not independent and should not be linearly superposed. Therefore, theoretical analyses with a single driving frequency [8–10, 16] are not directly applicable to the oceanic environment, where many tidal components exist.

VII. ACKNOWLEDGEMENTS

We thank Bruce Rodenborn and Yurun Liu for their help to set up the experiment. This work was supported by the Office of Naval Research Quantum Optics Initiative Grant No. N00014-03-1-0639.

[1] C. Wunsch and R. Ferrari, "Vertical mixing, energy, and the general circulation of the ocean," Annu. Rev. Fluid Mech. **36**, 281 (2004).

[2] J. R. Apel, *Principles of Ocean Physics* (Academic Press, 1987).

[3] C. Garrett and E. Kunze, "Internal tide generation in the deep ocean," to appear in Ann. Rev. Fluid Mech. (2007).

[4] P. K. Kundu and I. M. Cohen, *Fluid Mechanics* (Elsevier, 2004).

[5] J. Marotzke, "Abrupt climate change and thermohaline circulation: Mechanisms and predictability," Proc. Natl. Acad. Sciences **97**, 1347 (2000).

[6] S.R. Jayne, LC. St. Laurent, "Parametrizing tidal dissipation over rough topography," Geophys. Res. Lett. **28**, 811 (2001).

[7] T.H. Bell, "Lee waves in stratified flow with simple harmonic time dependence," J. Fluid Mech. **67**, 705 (1975).

[8] N.J. Balmforth, G.R. Ierley and W.R. Young, "Tidal conversion by nearly critical topography," J. Phys. Ocean. **32**, 2900 (2002).

[9] D.G. Hurley and G. Keady, "The generation of internal waves by vibrating elliptic cylinders. Part 2. Approximate viscous solution," J. Fluid Mech. **351**, 119 (1997).

[10] D. G. Hurley, "The generation of internal waves by vibrating elliptic cylinders. Part 1: Inviscid solution," J. Fluid Mech. **351**, 105 (1997).

[11] L. St. Laurent, S. Stringer, C. Garrett, and D. Perrault-Joncas, "The generation of internal tides at abrupt topography," Deep-Sea Res. I **50**, 987 (2003).

[12] B. R. Sutherland, S. B. Dalziel, G. O. Hughes, and P. F. Linden, "Visualisation and measurement of internal waves by 'synthetic schlieren.' Part 1: Vertically oscillating cylinder," J. Fluid Mech. **390**, 93 (1999).

[13] B. R. Sutherland and P. F. Linden, "Internal Wave Excitation by a Vertically Oscillating Elliptical Cylinder," Phys. Fluids **14**, 721 (2002).

[14] D. E. Mowbray and B. S. H. Rarity, "A theoretical and experimental investigation of the phase configuration of internal waves of small amplitude in a density stratified liquid," J. Fluid Mech. **28**, 1 (1967).

[15] N.H. Thomas and T.N. Stevenson, "A similarity solution of viscous internal waves," J. Fluid

Mech. **54**, 495 (1972).

[16] S.G. Llewellyn-Smith, W.R. Young, "Tidal conversion at a very steep ridge," J. Fluid Mech. **495**,175 (2003).

[17] F. Petrelis, S. G. Llewellyn Smith, and W.R. Young, Tidal conversion at a submarine ridge, J. Phys. Ocean, **36,** 1053 (2006).

[18] G. Oster, "Density Gradients," Sci. Am. **213**, 70 (1965).

[19] C. Staquet and J. Sommeria,"Internal gravity waves: From Instabilities to Turbulence," Annu. Rev. Fluid Mech. **34**, 559 (2002).

[20] A. Tabaei, T.R. Akylas and K.G. Lamb, "Nonlinear effects in reflecting and colliding internal wave beams," J. Fluid Mech. **526**, 217 (2005).

[21] K.G. Lamb, "Nonlinear interaction among internal wave beams generated by tidal over supercritical topography," Geophys. Res. Lett. **31**, L09313 (2004).

[22] T. Gerkema, C. Staquet and P. Bouruet-Aubertot, Decay of semi-diurnal internal tide beams due to sub-harmonic resonance. Geophys. Res. Lett. **33**, L08604 (2006).

[23] T. Gerkema, C. Staquet and P. Bouruet-Aubertot, "Non-linear effects in internal-tide beams, and mixing," Ocean Modelling **12**, 302 (2006).

[24] D. A. Aguilar and B. R. Sutherland, "Internal Wave Generation over Rough Topography," Phys. Fluids **18**, 066603 (2006).

[25] W. T. Welch, P. Smolarkiewicz, R. Rotunno, and B. A. Boville, "The large-scale effects of flow over periodic mesoscale topography," J. Atmos. Sci. **58**, 1477 (2001).

[26] A. Fincham and G. Delerce, "Advanced optimization of correlation imaging velocimetry algorithms," Exp. Fluids **29**, S13 (2000).

[27] T. Peacock and A Tabaei, "Visualization of nonlinear effects in reflecting internal wave beams," Phys. Fluids **17**, 061702 (2005).

[28] L. Gostiaux, T. Dauxois, H. Didelle, J. Sommeria and S. Viboux, "Quantitative laboratory observations of internal wave reflection on ascending slopes," Phys. Fluids **18**, 056602 (2006).

[29] L. Rosenhead, *Laminar Boundary Layers* (Oxford University Press, 1963).

[30] G. K. Batchelor, *An Introduction to Fluid Dynamics* (Cambridge University Press 1967).